Sintering effect on microstructural evolution and mechanical properties of spark plasma sintered Ti matrix composites reinforced by reduced graphene oxides

L.L. Dong [a], B. Xiao [a, b], Y. Liu [a], Y.L. Li [a], Y.Q. Fu[c],

Y.Q. Zhao[a], Y.S. Zhang [a, *]

[a] Advanced Materials Research Central, Northwest Institute for Nonferrous Metal Research, Xi'an 710016, China

[b] School of Materials Science and Engineering, Northwestern Polytechnical University, Xi'an 710072, China

[c] Faculty of Engineering and Environment, Northumbria University, Newcastle upon Tyne, NE1 8ST, UK.

Abstract:

Ti matrix composites reinforced with 0.6 wt.% reduced graphene oxide (rGO) sheets were fabricated using spark plasma sintering (SPS) technology at different sintering temperatures from 800 ^{o}C to 1100 ^{o}C. Effects of SPS sintering temperature on microstructural evolution and mechanical properties of rGO/Ti composites were studied. Results showed that with an increase in the sintering temperature, the relative density and densification of the composites were improved. The Ti grains were apparently refined owing to the presence of rGO. The optimum sintering temperature

* Corresponding author:
E-mail addresses: y.sh.zhang@163.com, y.s.zhang@c-nin.com (Y.S. Zhang)

was found to be 1000 ^{o}C with a duration of 5 min under a pressure of 45 MPa in vacuum, and the structure of rGO was retained. At the same time, the reaction between Ti matrix and rGO at such high sintering temperatures resulted in uniform distribution of micro/nano TiC particle inside the rGO/Ti composites. The sintered rGO/Ti composites exhibited the best mechanical properties at the sintering temperature of 1000^{o}C, obtaining the values of micro-hardness, ultimate tensile strength, 0.2% yield strength of 224 HV, 535 MPa and 446 MPa, respectively. These are much higher than the composites sintered at the temperature of 900^{o}C. The fracture mode of the composites was found to change from a predominate trans-granular mode at low sintering temperatures to a ductile fracture mode with quasi-cleavage at higher temperatures, which is consistent with the theoretical calculations.

Keywords: Spark plasma sintering, Reduced graphene oxide, Ti matrix composites, Mechanical properties, Microstructure

1. Introduction

Graphene, firstly obtained in 2004 by K.S. Novoselov and A.K. Geim [1], has the potential to be used as attractive reinforcements for composite materials owing to its unique physical and mechanical properties such as good electrical (1.5×10^{4} $cm^{2}/V\ S$) [2], thermal (5×10^{3} $W/m\ K$) [3] and mechanical (1 TPa of Young's modulus and 130 GPa of tensile strength) properties [4]. Recently, graphene has been

widely used as an excellent reinforcement material for metal matrix composites (MMCs). Previous studies showed remarkable achievements in mechanical properties of Al, Cu, Mg and WCu matrix composites after reinforced with graphene [5-10]. For example, tensile strength of Cu matrix composites with an addition of 2.5 vol.% reduced graphene oxide (rGO) prepared by molecule level mixing and spark plasma sintering (SPS) reached up to 748 MPa [11]. Dong et al. fabricated the graphene/WCu composites doped with 1.0 wt.% graphene using a powder metallurgy process, and the hardness was improved up to 121% [12]. Rashad et al. found that Al-0.3 wt% graphene composites prepared by a semi-powder method followed by a hot extrusion process exhibited a 0.2% yield strength (YS) of 198 MPa (＋14.7%), an ultimate tensile strength (UTS) of 285 MPa (＋11.1%), a hardness of 90 HV (＋11.8%) and a lower failure strain of 9.68% (＋40.6%) [13].

Titanium (Ti) and its alloys have good properties such as light weight, high strength and modulus, high temperature and corrosion resistances, therefore, they are extensively used as structural engineering materials in aircrafts and automobiles industries [14]. However, their wider applications in many engineering industries are rather limited, which is mainly because under severe working conditions, their mechanical properties such as strength and hardness become poor. In order to improve the mechanical properties of Ti matrix composites, some hard particles, including TiC, TiB, TiN, SiC, ZrO_2, Al_2O_3 and Y_2O_3 et al., were often introduced into Ti matrix composites using various fabrication technologies [15-22]. Multi-wall CNTs were also used to reinforce Ti matrix composites, and the yield strength and ultimate tensile

strength of Ti matrix composites with these CNTs were improved by 40.4% and 11.4%, respectively, [23].

So far very few papers have reported the synthesis of graphene/Ti composites. Mu et al. discovered that an ultimate tensile strength of 887 MPa was achieved for 0.1wt.% graphene-Ti matrix composites via powder metallurgy and subsequent hot-rolling, and the strength of the composites was 54.2% higher than that of pure Ti [24-25]. Zhang et al. reported that 7.0wt.% TiC incorporated Ti matrix composites exhibited an outstanding ultimate compressive strength of 2.64 GPa and a yield strength of 1.93 GPa at room temperature, which were fabricated through reactions of graphene and Ti mixture powders using the SPS [26]. However, rather limited data are currently available on the effect of SPS temperature on the microstructures and properties of the Ti matrix composites reinforced with graphene or its related materials, but it is well-known that the sintering temperature has a significant influence on the densification behaviors, microstructural evolution and properties enhancement of matrix composites.

Therefore, the objective of this work is to investigate the microstructural evolution and mechanical properties of Ti matrix composites reinforced with rGO additives prepared using the SPS method at different sintering temperatures (i.e. 800 ^{o}C, 900 ^{o}C, 1000 ^{o}C, and 1100 ^{o}C). The microstructural evolution and mechanical properties after sintering at different temperatures were studied, and the strengthening sintering mechanism was discussed based on theoretical analysis.

2. Experimental procedure

2.1 Materials

Graphene oxide (GO) was purchased from Western Superconducting Technologies Co., Ltd., China. Fig. 1(a) is an SEM image of the GO which shows a crumpled sheet structure. Pure spherical Ti powder (with purity＞99.9% and a mean diameter of ~150 μm), as shown in Fig. 1(b), was used as the matrix materials. The image reveals that there is no agglomeration of Ti powder particles and they are spherical in shape.

2.2 Synthesis of rGO/Ti composites

In our proposed synthesis method, there were six key steps to fabricate the rGO/Ti composites based on the powder metallurgy route. (a) GO powders were added into pure water and ultrasonicated for about 30 min until they become a homogeneous brown solution, indicating that the GO was uniformly dispersed into pure water. (b) Pure Ti powders were added into GO solution, and mechanically stirred for 30 min to obtain a mixture slurry. (c) The mixture slurry was completely dried using vacuum oven. After fully dried the GO/Ti mixed powders were obtained. (d) SPS technology was chosen to fabricate the bulk rGO/Ti matrix composites attributing to its high heating rate and sintering efficiency. The obtained rGO/Ti mixed powders were loaded into a graphite mould with an internal diameter of 40 mm and a height of 60mm. (e) The mixed powders in the graphite mould were sintered at different temperatures (i.e. 800^{o}C, 900^{o}C, 1000^{o}C and 1100^{o}C) for 5 min under a pressure of 45 MPa in a vacuum atmosphere. The temperature was controlled with a

thermocouple placed in the graphite mould which was located 2 mm away from the sample. The heating rate was 100^{o}C/min. (f) The sample was cooled down to room temperature in the furnace.

2.3 Characterization

In order to characterize the presence and nature of the rGO in sintered composites, a Raman spectrometer (HR Evolution) was used, with a He-Ne laser (633 nm) operated with a power of 17 mW and a detector with 4 cm^{-1} from Kaiser Optical System (France). The scan range of the laser beam was from 500~3000 cm^{-1} at room temperature. The morphology investigations of rGO/Ti mixed powders and sintered composites were performed using a scanning electron microscope (SEM, JEOL JSM-6700F). Microstructural and phase changes of samples were investigated using an optical microscope (OM, Axio Vert A1, ZEISS) and X-ray diffractometer (XRD, Bruker D8 ADVANCE), respectively.

Hardness of samples was measured using a Vickers hardness tester (MVS-1000IMT2), with the applied load of 200 g and a holding time of 10 s. Each sample was measured at least 10 indentations to obtain an average value. The Vickers microhardness value was calculated using the following equation:

$$HV = 1.8544\frac{P}{d^2} \qquad (1)$$

in which P is the applied load (N) and d is the diagonal length of the indentation (mm).

The compressive/tensile tests were carried out at room temperature using an

MTS810 universal testing machine with a strain rate of 1×10^{-3} s^{-1}. At least three measurements were performed to acquire an average value. The tensile fracture surface morphologies and composition were characterized using the SEM equipped with an energy dispersive X-ray spectroscope (EDS). Fig. 3 shows the schematic diagram and macrophotograph of tensile samples, respectively.

3. Results and discussion

3.1 Mixed powders

SEM micrographs of GO/Ti composite powders are displayed in Fig. 4. The GO was effectively absorbed on the surfaces of spherical Ti powders, as shown in Fig. 4(a). Also, agglomeration of the GO was also observed, as shown in the red rectangle marked in Fig. (a). Fig. 4(b) is an enlarged view of this area, which suggests that the transparent and crumpled structure of the GO was not obvious, revealing that most of the GO sheets are attached to the surface of Ti matrix powders.

3.2 Microstructures of sintered rGO/Ti composites

Fig. 5 shows the optical micrographs of the rGO/Ti composites sintered at different temperatures using SPS. At sintered at a temperature of 800 ^{o}C, the grain boundaries of spherical Ti matrix and agglomerated rGOs (which are located in the pores between Ti – Ti particles) are clearly observed in the composites owing to the lower sintering temperature, as shown in Fig. 5(a). However, the Ti atoms in the composites can migrate effectively thus achieving a better densification with an

increase in the sintering temperature. On the other hand, rGO is often considered to be beneficial for grain refinement and hence it can improve the sintering behavior of metal matrix composites (such as Mg, Ti, WCu, and Al matrix composites). The grain refinement of Ti matrix composites is not obvious in Figs. 5(a)~(d), probably due to the fact that the observed samples were not pre-etched. Therefore, the tiny pores in the composites are relatively fewer (in Fig. 3(d)) for the samples sintered at a higher temperature.

Surface morphologies of the rGO/Ti composites were also investigated using SEM, and the results are shown in Fig. 6. At the low sintering temperature, all the rGO is clearly retained at the trigeminal boundaries of titanium particles, as shown in Figs. 6(a_1) and (b_1). Also, the pores existed between the rGO and Ti matrix is obvious as shown in Figs. 6(a_2) and (b_2) owing to the low diffusion activation energy at the sintering temperatures of 800^{o}C and 900^{o}C. It is noteworthy to point out that a layer of gray TiC (determined by EDS in Fig. 6(b_3)) coating is formed on the rGO sheets as shown in Fig. 6(b_2), which should improve the interfacial bonding strength between the rGO and Ti matrix if the sintering temperature and pressure are further increased. When the temperature is over 900^{o}C, the distinct Ti grain boundaries and pores are disappeared as can be observed from Figs. 6(c_1) and (d_1). Further densification takes place with an increase in the temperature to 1100 ^{o}C. In Figs. 6(c_2) and (d_2), some nano/micro TiC particles distributed in the Ti matrix are formed by reactions between Ti and rGO sheets. The formation of TiC will enhance the mechanical properties of composites, especially the hardness and strength.

In order to further study the C element (i.e. graphene) distribution in the rGO/Ti composites after sintered at 1000 ^{o}C. The SEM image and EDS mapping results are shown in Figs. 7(a) and (b_i). The C element is uniformly distributed on the surface of the Ti matrix. Agglomerated graphene are also founded at the Ti grain boundaries, which are related to in-situ formed TiC particles, as observed in Figs. 7(b_0)~(b_2).

The migration rate during the sintering can be expressed as follows [27]:

$$\varepsilon = \frac{d\varepsilon}{dt} = A\frac{\varphi\mu \mathrm{b}}{\mathrm{kT}}\left(\frac{b}{G}\right)^{p}\left(\frac{\sigma}{\mu}\right)^{\mathrm{n}} \qquad (2)$$

in which ε is the migration rate, t is the time (s), A is the constant, φ is the diffusion exponen, μ is the shear modulus, b is the Burgers vector, K is the boltzmann constant (1.38×10^{-23}J/K), T is the sintering temperature (K), G is the grain size (nm), σ is the microscopic stress (MPa), P is the grain size exponent, n is the effective stress. Generally, the migration of materials during SPS is similar with that of during high-temperature sintering, so the kinetics equation of SPS process can be written as [28]:

$$\frac{1}{D}\frac{dD}{\mathrm{d}t} = \frac{B\varphi\mu_{\mathrm{eff}}\mathrm{b}}{\mathrm{kT}}\left(\frac{b}{G}\right)^{\mathrm{p}}\left(\frac{\sigma_{\mathrm{eff}}}{\mu_{\mathrm{eff}}}\right)^{\mathrm{n}} \qquad (3)$$

in which D is instantaneous relative density (%), B is the constant, σ_{eff} is instantaneous compressive stress (MPa), and μ_{eff} is instantaneous shear stress (MPa).

According to Ashby [29], the instantaneous compressive stress can be shown as:

$$\sigma_{eff} = \frac{1-D}{(D-D_0)D^2}\sigma_{\mathrm{mac}} \qquad (4)$$

in which σ_{mac} is the 45MPa, D_0 is the relative density (40%).

The Young's modulus of porous material can be calculated according Eq. (5)

$$\frac{E_{eff}}{E_{th}} = 1 - \frac{P}{P_0} \qquad (5)$$

where E_{eff} is actual Young's modulus (GPa), E_{th} is Young's modulus the theoretical dense material (GPa), p=1-D is the actual porosity (%), P_0= 1-D_0 original porosity (%). μ_{eff} can be expressed using Eq. (6):

$$\mu_{eff} = \frac{E_{eff}}{2(1+\nu_{eff})} \qquad (6)$$

According to Eqs. (2)~(6), the kinetics equations of SPS process can then be further expressed as:

$$\frac{1}{\mu eff}\frac{1}{D}\frac{dD}{dt} = K\frac{-\frac{Q_d}{Rt}}{T}\left(\frac{b}{G}\right)^P\left(\frac{\sigma_{eff}}{\mu_{eff}}\right)^n \qquad (7)$$

$$\ln\left(\frac{1}{\mu_{eff}}\frac{1}{D}\frac{dD}{dt}\right) = n\ln\left(\frac{\sigma_{eff}}{\mu_{eff}}\right) + K_1 \qquad (8)$$

in which K is the constant, R is the gas constant (8.314 J/mol K), Q_d is the activation energy of surface diffusion (J). We assumed that $Y=\ln\left(\frac{1}{\mu_{eff}}\frac{1}{D}\frac{dD}{dt}\right)$, $X=\ln\left(\frac{\sigma_{eff}}{\mu_{eff}}\right)$, thus the Eq. (8) can be rewritten as $Y=nX+K_1$. The values of stress exponent n calculated at different temperatures are plotted and fitted in Fig. 8. As can be seen from Fig. 8, the effective pressure index n is about 0.5 at the lower sintering temperatures (800^{o}C and 900 ^{o}C). However, with an increase in the sintering temperature to 1000 ^{o}C and 1100 ^{o}C, the value of n increases to 1.2 and 1.56, respectively. The densification mechanism is gradually changed into the simultaneous actions of pure diffusion densification and high temperature creep densification. While with an increase in the holding time, the value of n is increased from 1.23 at the temperature of 800 ^{o}C to 2.18 at the temperature of 1100 ^{o}C. According to references [27-29], when n is

approximately 2, the densification mechanism is mainly considered to be high temperature creep. In this work, the n values at different temperatures with a sintering pressure of 45 MPa are higher than those reported in the literature [30-32], owing to the increased sintering activation of Ti matrix enhanced by the rGO. The similar phenomenon and sintering activation mechanism have been reported in WCu matrix composites in our previous work [10, 12].

The XRD patterns of samples sintered at different temperatures are shown in Fig. 8. Only Ti phase can be observed in the pure Ti sample (cf JCPDS file No. 01-1197). However, the weak diffraction peak at ~ 40.3° corresponding to TiC phase was observed in all the sintered rGO/Ti composites (cf JCPDS file No. 32-1383). The intensity of the TiC phase increases with an increase in the sintering temperature, as showed in the inset of Fig. 9. It reveals that the chemical reaction between Ti and rGO occurred during SPS process when the sintered temperature exceeded 800 ^{o}C. The standard free energy (ΔG) of TiC formation from the reaction between Ti and carbon can be expressed using the following equation [33]:

$$\Delta G=-184571.8+41.382T-5.042TlnT+2.425\times10^{-3}T^{2}-9.79\times10^{5}/T \quad (T<1939K) \quad (9)$$

in which ΔG (kJ/mol) is the free energy, T (K) is the reaction temperature. According to Eq. (1), the ΔG values of TiC formation at different temperatures (e.g., 800 ^{o}C, 900 ^{o}C, 1000 ^{o}C and 1100 ^{o}C) in this work are -176.04 kJ/mol, -175.33 kJ/mol, -174.61 kJ/mol and -157.75 kJ/mol, respectively. It can be concluded that the TiC particles were *in-situ* formed during SPS. Significant enhancement of mechanical properties of metal matrix composites was reported after they were reinforced with TiC [34-36].

For example, Jeyasimman et al. found that the hardness of Al matrix composites reinforced with 2 wt.% TiC particles was 1180 MPa, which was four times higher than that of pure Al6061 [37]. The rGO diffraction peaks were not detected in experiments owing to the lower content of the rGO in the composites. Notably, the intensities of the Ti peaks in the rGO/Ti composites sintered at different temperatures are all broader and weaker than those of the pure Ti, mainly owing to the grain refinement effect after adding the rGO.

In order to further characterize the existence of rGO in the composites, Raman spectroscopy was conducted and the obtained spectra of the composites sintered at different temperatures with the scanning size of 60×60 μm^2 are shown in Fig. 10. In Raman mapping results, the brighter the color, the stronger the reduced graphene oxide signal [38]. It can be concluded that the rGO contents in composites increase with an increasing SPS temperature. However, in Fig. 10(d), the rGO signal is extremely feeble in Raman mapping, which would means lots of rGO react with Ti matrix, which further validates the previous analysis (Fig. 6). Fig. 10(e) is the Raman spectra of point a, b, c, and d which is one of the four mapping region, respectively. Generally, the D band in carbon materials is associated with the signal of the defects introduced in the structure, whereas the G band is associated with the degree of graphitization, and the ratio of I_D/I_G reveals the structural defects and sizes of graphene materials. As shown in Fig. 10(e), all the sintered rGO/Ti composites exhibit an intense D band at ~ 1350 cm^{-1} and G band at ~ 1595 cm^{-1}, also the intensities of D and G bands become much higher with an increase in sintering temperature except for

1100 ^{o}C. The obtained ratios of I_D/I_G are listed in the inset of Fig. 10(e), and they are increased from 1.26 to 1.56 when the temperature is increased to 1000 ^{o}C, which suggests that the graphene structure has been degraded. However, the broad 2D band at 2680 cm^{-1} for Ti-1000-0.6C sample is clearly observed in Fig. 10, implying that the GO was reduced at 1100^{o}C and there are still remained intact reduced graphene structures in the rGO/Ti composites. To our knowledge, the existence of 2D peak is often used to confirm the presence of graphene and determine the number of graphene layers. For a single layered graphene, the 2D peak is quite narrow and relatively sharp, however it becomes broadened and displays peak-splitting with an increase in the number of graphene layers [39]. The rGO in this work clearly are multiple layer structures after the SPS. However, the intensity of 2D peak of the sample of Ti-1000-0.6C is much higher than those of others, suggesting that the structure of rGO is still retained in the sintered composites of the Ti-1000-0.6C after SPS.

3.3 Mechanical properties of sintered rGO/Ti composites

Fig. 11 shows the micro-hardness of 0.6 wt.% rGO/Ti composites sintered at different temperatures. The Ti-800-0.6C sample has a low hardness of 186.8 HV owing to its lower relative density (In Fig. 5(a)). The micro-hardness of samples increases with an increase in the sintering temperature. The microhardness value is 224 HV for the sample sintered at the temperature of 1000 ^{o}C, however, the hardness decreases slightly to the value of 213 HV when the SPS temperature exceeds 1000 ^{o}C.

The mechanical properties of the 0.6 wt.% rGO/Ti composite samples are

presented in Fig. 12. The plots reveal that a remarkable strength improvement was obtained at the sintering temperature of 1000 ^{o}C, with YS and UTS values of 565 MPa and 2.05 GPa, respectively, as shown in Fig. 12(a), which are much higher than those of samples sintered at 800^{o}C. The tensile stress-strain curves and the corresponding tensile properties of composites sintered at different temperatures are also shown in Figs. 12(b) and 12(c). The poorest tensile properties (i.e., UTS=192MPa, elongation=0%) were obtained for the specimen fabricated at the temperature of 800 ^{o}C, which is mainly due to inadequate atomic diffusion and lower relative density at such a low sintering temperature. As shown in Fig. 12(c), the strength and elongation of the rGO/Ti composites increase with the temperature, however, the YS of samples becomes slowly decreasing when the sintering temperature reaches 1100 ^{o}C. The main reasons for the improved elongation with temperature are as follows: firstly the defects (e.g. pores) are eliminated at the higher sintering temperature under the same pressure, which reduces the stress concentration in the tensile testing. On the other hand, a stronger bonding of rGO and Ti matrix is formed at the temperature higher than 800 ^{o}C. Hence, it can be concluded that the variations of compression/tensile properties with the sintering temperature has a similar trend with those of microhardness, which are linked with the microstructural changes of the samples.

3.4 Fracture morphology of sintered rGO/Ti composites

SEM fracture morphologies of the rGO/Ti composites sintered at different

temperatures are shown in Fig. 13. A number of rock-candy shapes of grains and numerous pores are clearly observed at the low sintering temperatures (e.g., 800^{o}C and 900^{o}C), as described in Figs. 13(a) and 13(b), which suggests ineffective sintering process occurred at such a low SPS temperature. This can be confirmed from the trans-granular fracture surfaces of the sample as shown in Figs. 13(a) and 13(b). Some layered structure of un-sintered rGO at the Ti-Ti grain boundaries can be observed. With an increase in the sintering temperature, the fracture morphology of composites is significantly changed. The large size pores among the Ti grain boundaries disappear as shown in Figs. 13(c) and 13(d). However, some dimples with an average size of 8 μm are exhibited on the fracture surface of the composites, and a ductile fracture mode with a feature of quasi-cleavage is observed, which is corresponding to a high toughness value for the Ti-1100-0.6C composites (in Fig. 12(c)). Further observation in Fig. 13(d) reveals the presence of pull-out of the TiC phase (determined by the EDS results in Fig. 13(e)), showing the trans-granular fracture phenomenon. The presence of TiC particles is actually beneficial for the further improvement of mechanical properties for the composites [40]. This is consistent with the analysis and conclusions obtained in Section 3.3.

4. Conclusions

Ti matrix composites containing 0.6 wt.% rGO sheets were successfully prepared using the SPS at various sintering temperatures. The effects of SPS sintering temperature on the microstructure and mechanical properties of rGO/Ti composites

were studied in this work. The following conclusions can be obtained:

(1) With an increase in the sintering temperature, the relative density and densification were improved, and the Ti grains were refined owing to the presence of rGO. However, the optimum sintering temperature was 1000 ^{o}C for 5 min under 45 MPa in a vacuum, and the structure of rGO can be retained. The reaction between Ti matrix and rGO has occurred, forming micro/nano TiC particle uniformly dispersed in the rGO/Ti composites at the high sintering temperature of 1000^{o}C.

(2) The sintered rGO/Ti composites exhibited the best comprehensive properties at the sintering temperature of 1000 ^{o}C. The micro-hardness, ultimate tensile strength and 0.2% yield strength sintered at the temperature of 1000 ^{o}C were 224 HV, 535 MPa and 446 MPa, respectively, which were higher at 24.5%, 12.9% and 11.5%, respectively, as compared to those of the composites sintered at the temperature of 900 ^{o}C.

(3) The fracture mode of composites changed from predominately trans-granular mode at low sintered temperature to ductile fracture mode with quasi-cleavage at higher temperature. The changes of fracture modes were consistent with the theoretical calculations.

Acknowledgments

This work was supported by the National Security Major Basic Research Plan of China and the funded by Northwest Institute for Nonferrous Metal Research (K1652-11), National Natural Science Foundation of China (Grant No. U1737108),

the Natural Science Basic Research Plan in ShaanXi Province of China (2017ZDJC-19), Innovation team in key areas of Shaanxi Province (2016KCT-30) and UK Newton Mobility Grant (IE161019) through Royal Society and the National Natural Science Foundation of China, as well as Royal academy of Engineering UK-Research Exchange with China and India.

Reference

[1] K.S. Novoselov, A.K. Geim, S.V. Morozov, D. Jiang, Y. Zhang, S.V. Dubonos, I.V. Grigorieva, A.A. Firsov, Electric field effect in atomically thin films, science 306(2004) 666-669.

[2] F. Schedin, A. K. Geim, S. V. Morozov, E. W. Hill, P. Blake, M. L. Katsnelson, K. S. Novoselov, Detection of individual gas molecules adsorbed on graphene, Nat. Mater. 6 (9) (2007) 652-655.

[3] A. A. Baladin, S. Ghosh, W. Bao, I. Calizo, D. Teweldebrhan, F. Miao, C. N. Lau, Superior thermal conductivity of single layer graphene, Nano Lett. 8 (3) (2008) 902 - 907.

[4] C. Lee，X. Wei，J. W. Kysar, J. Hone, Measurement of the elastic properties and intrinsic strength of monolayer graphene, Science 321 (5887) (2008) 385 - 388.

[5] J. Dutkiewicz, POzga, W. Maziarz, J. Pstruś, B. Kania, P. Bobrowski, J. Stolarsk, Microstructure and properties of bulk copper matrix composites strengthened with various kinds of graphene nanoplatelets, Mater. Sci. Eng. A 628 (2015) 124–134

[6] F.Y. Chen, J.M. Ying, Y.F. Wang, S.Y. Du, Z.P. Liu, Q. Huang, Effects of graphene content on the microstructure and properties of copper matrix composites, Carbon 96 (2016) 836-842

[7] F. Khodabakhshi, S.M. Arab, P. Švec, A.P. Gerlich, Fabrication of a new Al-Mg/graphene

nanocomposite by multi-pass friction-stir processing: Dispersion, microstructure, stability, and strengthening, Mater. Charact. 132(2017) 92-107

[8] R. Pérez-Bustamante, D. Bolaños-Morales, J. Bonilla-Martínez, I. Estrada-Guel, R. Martínez-Sánchez, Microstructural and hardness behavior of graphene-nanoplatelets/aluminum composites synthesized by mechanical alloying, J. Alloy. Compd. 615 (2014) S578-S582.

[9] L.L. Dong, W.G. Chen, N. Deng, C.H. Zheng, Investigation on arc erosion behaviors and mechanism of W70Cu30 electrical contact materials adding graphene, J. Alloy. Compd. 696 (2017) 923-930.

[10] W.G. Chen, L.L. Dong, J.J. Wang, Y. Zuo, Y.Q. Fu. Synergistic enhancing effect for mechanical and electrical properties of tungsten copper composites using spark plasma infiltrating sintering of copper-coated graphene, Sci. Rep.-UK 2017, 7: 17836-17845.

[11] Z.Y. Yang, L.D. Wang, Z.D. Shi, M. Wang, Y. Cui, B. Wei, S.C. Xu, Y.P. Zhu, W.D. Fei, Preparation mechanism of hierarchical layered structure of graphene/copper composite with ultrahigh tensile strength, Carbon 127 (2018) 329-339.

[12] L.L. Dong, W.G. Chen, C.H. Zheng, N. Deng, Microstructure and properties characterization of tungsten-copper composite materials doped with graphene, J. Alloy. Compd. 695 (2017): 1637-1646.

[13] M. Rashada, F.S. Pan, A.T. Tang, M. Asif, Effect of graphene nanoplatelets addition on mechanical properties of pure aluminum using a semi-powder method, Prog. Nat. Sci. - Mater. 24(2014) 101-108.

[14] G. Lütjering, J.C. Williams, A. Gysler, Titanium engineering materials and progresses, vol. 379, 2nd ed. Berlin: Springle; 2007.

[15] C.J. Zhang, F.T. Kong, S.L. Xiao, E.T. Zhao, L.J. Xu, Y.Y. Chen, Evolution of microstructure and tensile properties of in situ titanium matrix composites with volume fraction of (TiB + TiC) reinforcements, Mat. Sci. Eng. A 548 (2012) 152- 160.

[16] Z. Yan, F. Chen, Y. Cai, Y. Zheng, Microstructure and mechanical properties of in-situ synthesized TiB whiskers reinforced titanium matrix composites by high-velocity compaction, Powder Technol. 267 (2014) 309-314.

[17] S.D. Luo, Q. Li, J. Tian, C. Wang, M. Yan, G.B. Schaffer, et al., Self-assembled, aligned TiC nanoplatelet-reinforced titanium composites with outstanding compressive properties, Scr. Mater. 69 (2013) 29-32.

[18] S. Li, K. Kondoh, H. Imai, B. Chen, L. Jia, J. Umeda, Microstructure and mechanical properties of P/M titanium matrix composites reinforced by in-situ synthesized TiC-TiB, Mater. Sci. Eng. A 628 (2015) 75-83.

[19] E. Lascoste, C. Arvieu, J.M. Quenisset, Correlation between microstructures of SiC-reinforced titanium matrix composite and liquid route processing parameters, J. Mater. Sci. 50 (2015) 5583-5592.

[20] C. Han, Y.C. Li, X.G. Liang, L.P. Chen, N. Zhao, X.K. Zhu, Effect of composition and sintering temperature on mechanical properties of ZrO_2 particulate-reinforced titanium-matrix composite, Trans. Nonferr. Metals Soc. China 22 (2012) 1855-1859.

[21] A. Shafiei-Zarghani, S.F. Kashani-Bozorg, A.P. Gerlich, Strengthening analyses and mechanical assessment of Ti/Al_2O_3 nano-composites produced by friction stir processing, Mater. Sci. Eng. A 631 (2015) 75-85.

[22] V. Castro, T. Leguey, A.Muñoz, M.A. Monge, R. Pareja, Relationship between hardness and

tensile tests in titanium reinforced with yttria nanoparticles, Mater. Sci. Eng. A 400 (2005) 345-348.

[23] S.F. Li, B. Sun, H. Imai, T. Mimoto, K. Kondoh, Powder metallurgy titanium metal matrix composites reinforced with carbon nanotubes and graphite, Compos. Part A-Appl. S 48(2013) 57-66.

[24] X.N. Mu, H.M. Zhang, H.N. Cai, Q.B. Fan, Z.H. Zhang, Y. Wu, Z.J. Fu, D.H. Yu. Microstructure evolution and superior tensile properties of low content graphene nanoplatelets reinforced pure Ti matrix composites, Mat. Sci. Eng. A 687 (2017) 164-174;

[25] X.N. Mu, H.N. Cai, H.M. Zhang, Q.B. Fan, Z.H. Zhang, Y.Wu, Y.X. Ge, D.D.Wang Interface evolution and superior tensile properties of multi-layer graphene reinforced pure Ti matrix composite, Mat. Des. 140 (2018) 431-441.

[26] X.J. Zhang, F. Song, Z.P. Wei, W.C. Yang, Z.K. Dai, Microstructural and mechanical characterization of in-situ TiC/Ti titanium matrix composites fabricated by graphene/Ti sintering reaction, Mat. Sci. Eng. A 705 (2017) 153-159.

[27] T. Sugita, J.A. Pask, Creep of doped polycrystalline Al_2O_3, J. Am. Ceram. Soc. 1970, 53(11) 609- 613.

[28] C. Ting, H. Lu, Hot-pressing of magnesium aluminate spinel-I. Kinetics and densification mechanism, Acta Mater. 1999, 47(3): 817−830.

[29] R. Chaim, O.R. Bar-hama, Densification of nanocrystalline NiO ceramics by spark plasma sintering, Mat. Sci. Eng. A 527 (3) (2010) 462−468.

[30] G.H. Liu, T.C. Yuan, R.D. Li, Q.G. Weng, J.W. Yuan, Effect of spark plasma sintering temperature on densification kinetics and microstructure during pure titanium phase transition,

Mat. Sci. Eng. Powder Metall. 22(5) (2017) 650-655

[31] Q.G. Weng, R.D. Li, L.B. Zhou, T.C. Yuan, Y.H. He, H. Wu, Densification dynamics and microstructure evolution behaviors of spark plasma sintering of titanium powders, Mat. Sci. Eng. Powder Metall. 20(1) (2015) 149-154.

[32] G. Bernard-Granger, A. Addad, G. Fantozzi, G. Bonnefont, C. Guizard, D. Vernat, Spark plasma sintering of a commercially available granulated zirconia powder: Comparison with hot-pressing, Acta Mater. 58 (2010) 3390-3399

[33] Knacke, O. Kubaschewski, K. Hesselmann, Thermaochemical properties of inorganic substance, vol. 264, 2nd ed. New York: Springer-Verlag; 1991. p.2501–104.

[34] V.A. Popov, E.V. Shelekhova, A.S. Prosviryakov, M.Y. Presniakov, B.R. Senatulin，A.D. Kotov, M.G. Khomutov, Particulate metal matrix composites development on the basis of in situ synthesis of TiC reinforcing nanoparticles during mechanical alloying, J. Alloy. Compd. 707 (2017) 365-370.

[35] F. Wang, Y. Li, X. Wang, Y. Koizumi, Y. Kenta, A. Chiba, In-situ fabrication and characterization of ultrafine structured Cu-TiC composites with high strength and high conductivity by mechanical milling, J. Alloy. Compd. 657 (2016) 122-132.

[36] H. Kwon, M. Takamichi, A. Kawasaki, M. Leparoux, Investigation of the interfacial phases formed between carbon nanotubes and aluminum in a bulk material Materials, Chem. Phys. 138 (2013) 787-793.

[37] D. Jeyasimman, S. Sivasankaran, K. Sivaprasad, R. Narayanasamy, R.S. Kambali, An investigation of the synthesis, consolidation and mechanical behaviour of Al 6061 nanocomposites reinforced by TiC via mechanical alloying, Mat. Des. 57 (2014) 394–404.

[38] X. Yu, Z. Zhang, F. Liu, Y. Ren, Synthesis of transfer-free graphene on cemented carbide surface, Sci. Rep.-UK, 8 (2018) 4759-4568.

[39] M.S. Dresselhaus, A. Jorio, M. Hofmann, G. Dresselhaus, R. Saito, Perspectives on carbon nanotubes and graphene Raman spectroscopy, Nano Lett. (10) (2010) 751–758.

[40] K. Kondoh, T. Threrujirapapong, H. Imai, J. Umeda, B. Fugetsu, Characteristics of powder metallurgy pure titanium matrix composite reinforced with multi-wall carbon nanotubes, Compos. Sci. Technol. 69 (2009) 1077-1081.

List of Tables captions:

Fig. 1 SEM micrographs of the source materials. (a) graphene oxide, (b) Ti powder.

Fig. 2 Schematic illustration of fabrication process of the rGO/Ti composites using SPS.

Fig. 3 (a) Schematic diagram and (b) photo of a tensile sample.

Fig. 4 (a) SEM images of GO/Ti mixture powders and (b) an enlarged view of red rectangle position marked in 4(a).

Fig. 5 Optical micrographs of 0.6 wt.% rGO/Ti composite prepared at various temperature (a) 800^{o}C, (b) 900^{o}C, (c) 1000^{o}C and (d) 1100^{o}C.

Fig. 6. SEM images of 0.6 wt.% rGO/Ti composites prepared at different temperatures (a) 800^{o}C, (b) 900^{o}C, (c) 1000 ^{o}C and (d) 1100 ^{o}C, respectively.

Fig. 7 SEM image (a) and (b_0)~(b_2) EDS mapping results of rGO/Ti composites SPS at 1000 ^{o}C.

Fig. 8 Effective pressure index (n) obtained from equation (8), presented by the slope

of different fitted curves.

Fig. 9 XRD patterns of the rGO/Ti composites sintered at the different temperature.

Fig. 10 Raman mapping of the 0.6wt.% rGO/Ti matrix SPSed composites at different temperature (size of 60×60 μm^2): (a) 800^oC; (b) 900^oC; (c) 1000^oC; (d) 1100^oC, (e) The Raman spectra of point a, b, c, and d which is one of the four mapping region, respectively.

Fig. 11 Micro-hardness of rGO/Ti composites at different sintered temperatures.

Fig. 12 (a) Compressive stress-strain curves, (b) tensile stress-strain curves and (c) the corresponding tensile properties of 0.6 wt.% rGO/Ti composites sintered at different temperatures.

Fig. 13 SEM fracture morphology of rGO/Ti composites sintered at different temperatures: (a) 800 ^oC, (b) 900 ^oC, (c) 1000 ^oC, (d) 1100 ^oC, respectively. (e) EDS result of the red arrow positions marked in Fig. 13 (d).

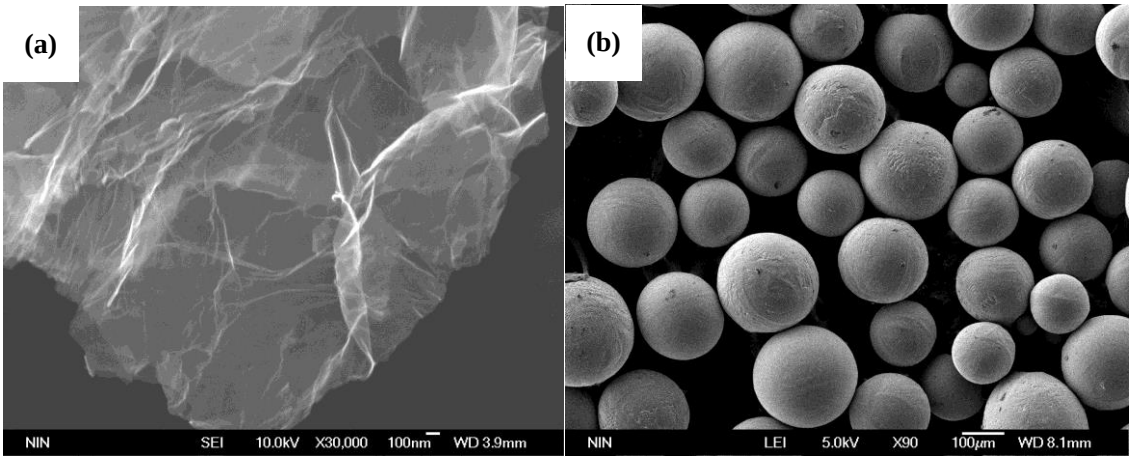

Fig. 1 SEM micrographs of the source materials. (a) graphene oxide, (b) Ti powder.

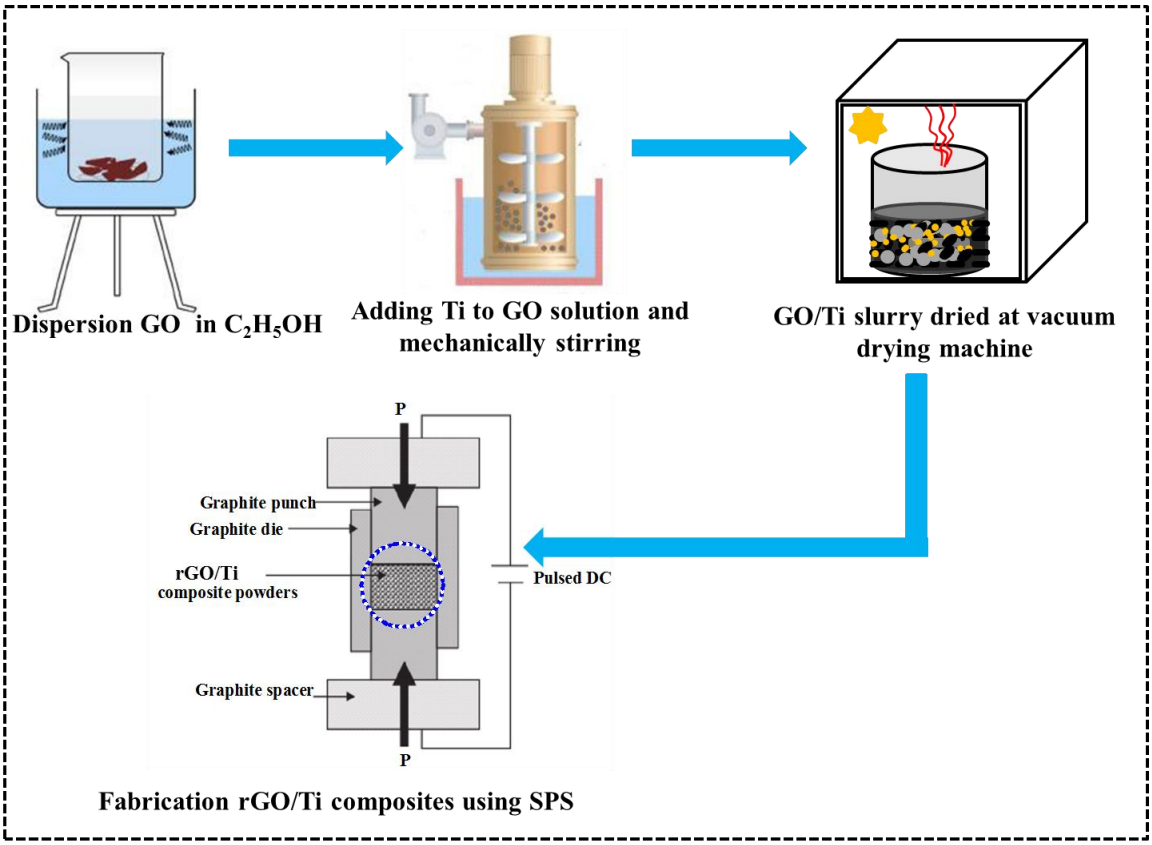

Fig. 2 Schematic illustration of fabrication process of the rGO/Ti composites using SPS.

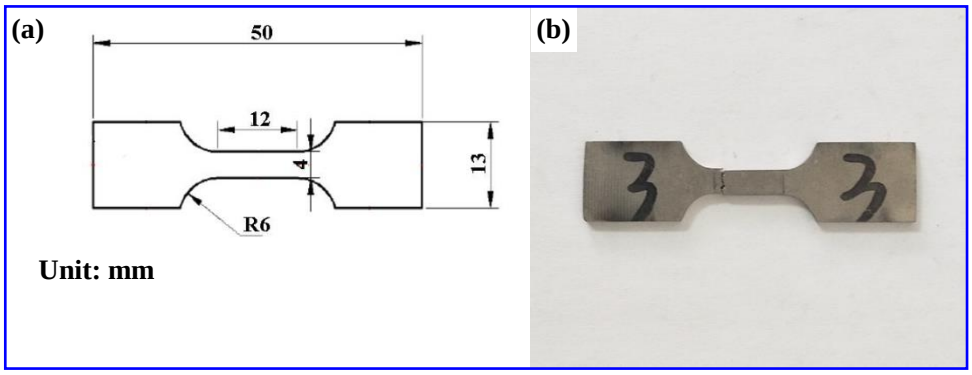

Fig. 3 (a) Schematic diagram and (b) photo of a tensile sample.

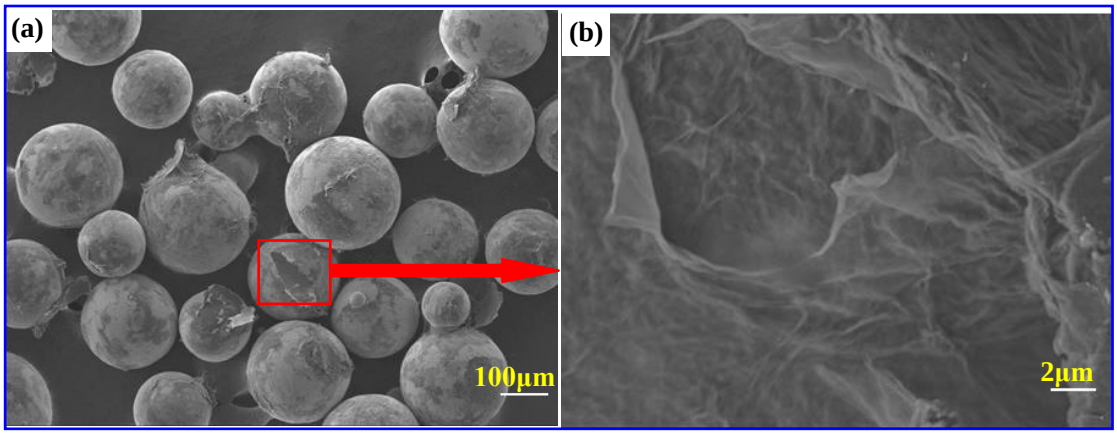

Fig. 4 (a) SEM images of GO/Ti mixture powders and (b) an enlarged view of red rectangle position marked in 4(a).

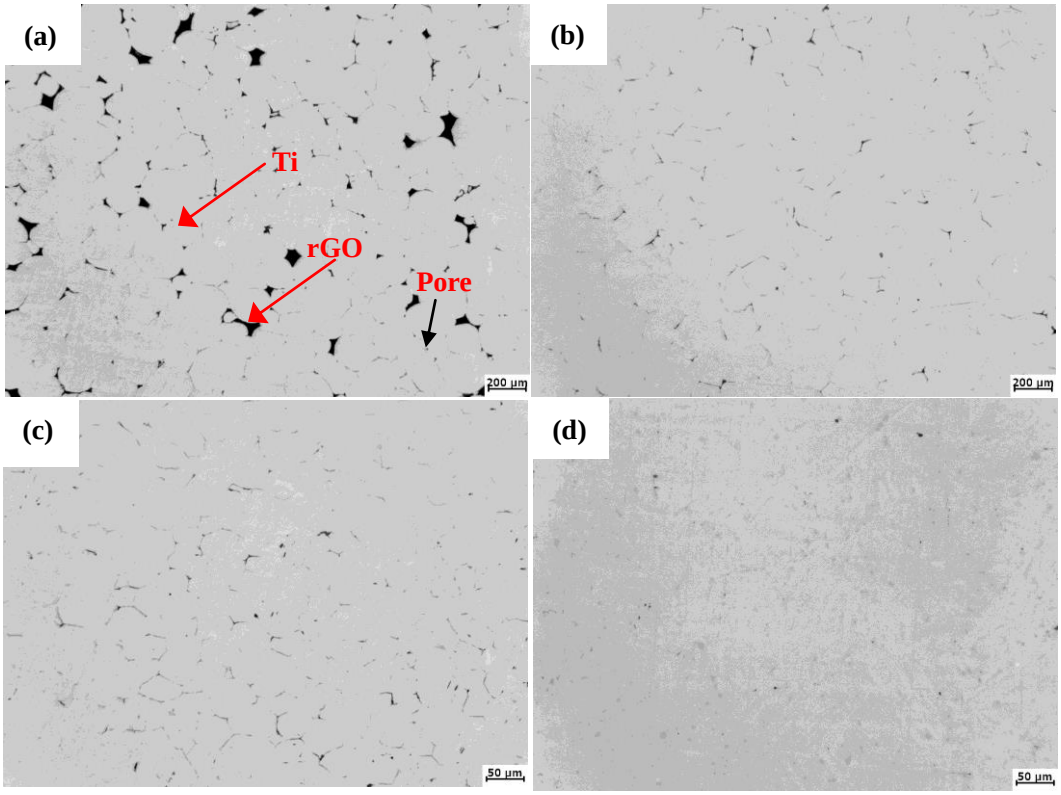

Fig. 5 Optical micrographs of 0.6 wt.% rGO/Ti composite prepared at various temperature (a) 800^{o}C, (b) 900^{o}C, (c) 1000^{o}C and (d) 1100^{o}C.

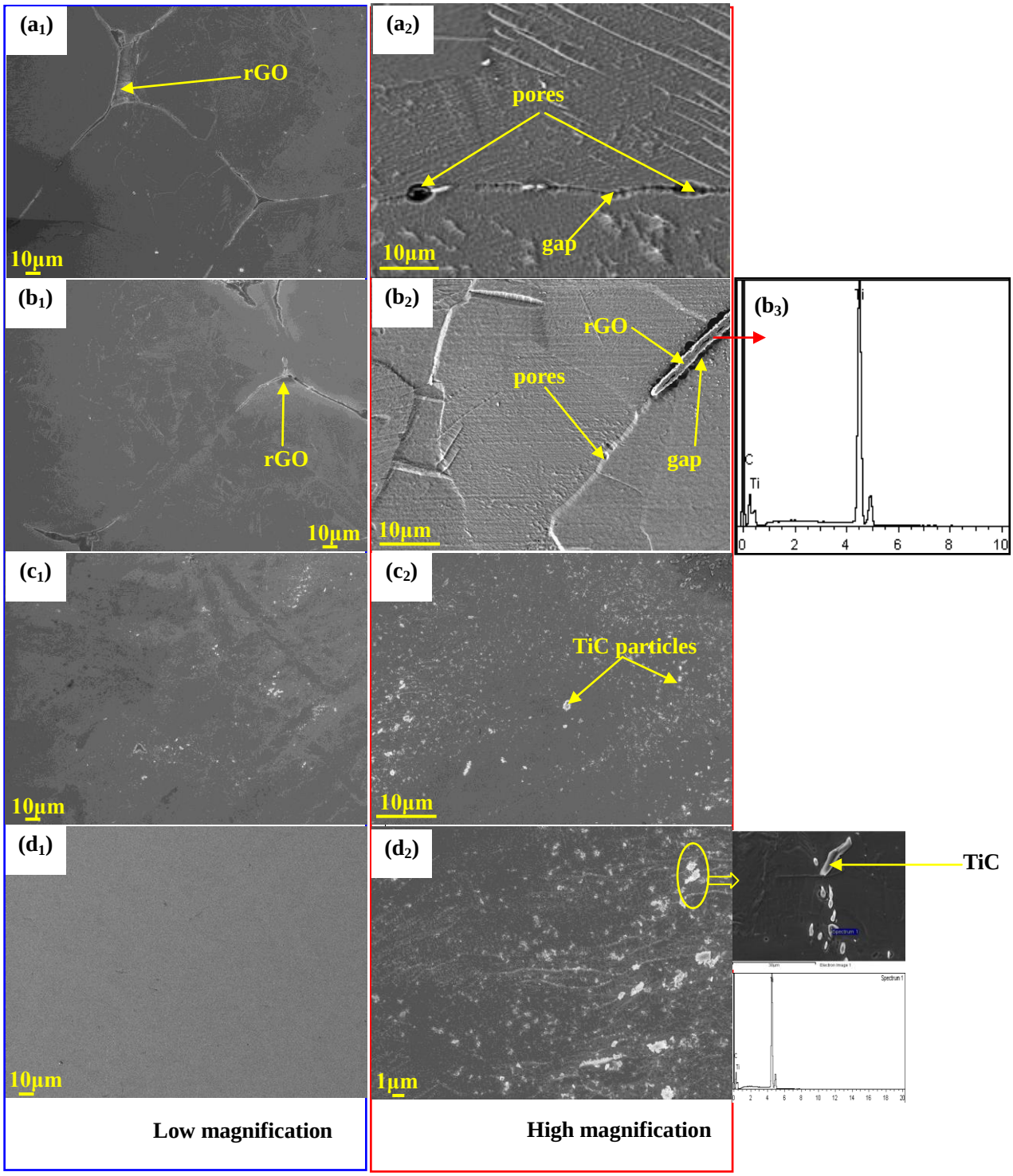

Fig. 6 SEM images of 0.6 wt.% rGO/Ti composites prepared at different temperatures

(a) 800^{o}C, (b) 900^{o}C, (c) 1000 ^{o}C and (d) 1100 ^{o}C, respectively.

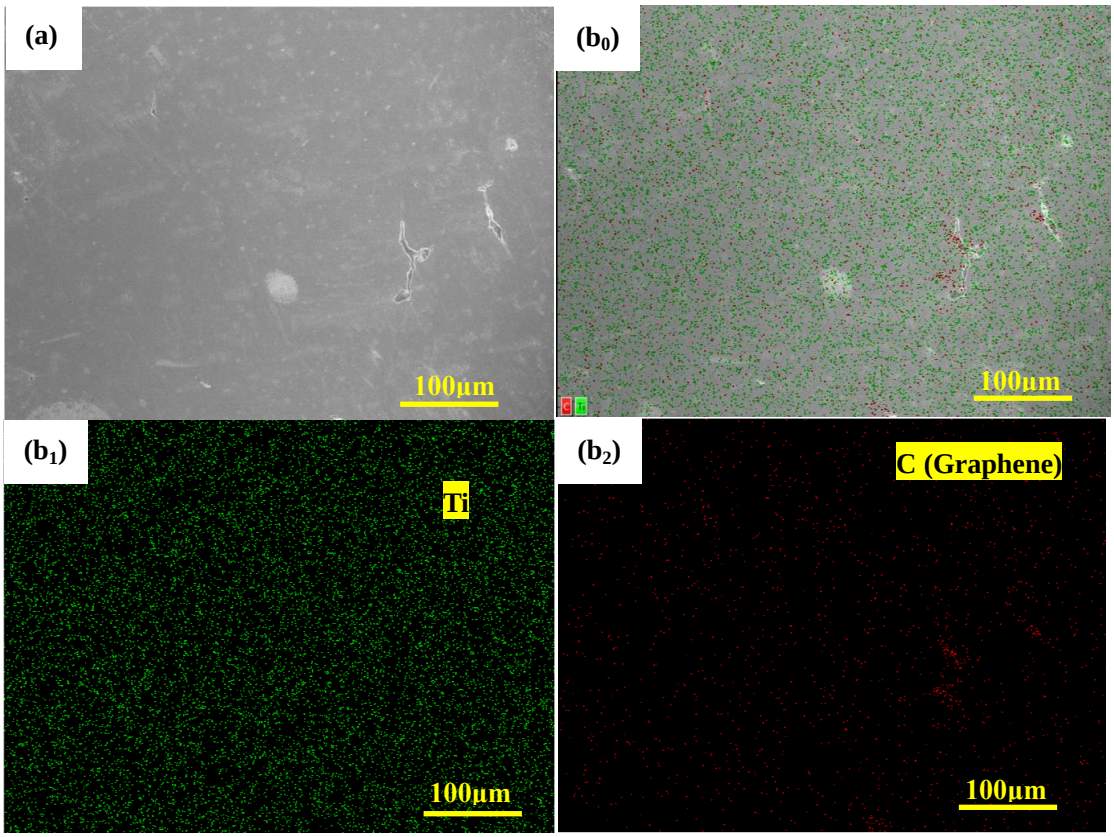

Fig. 7 SEM image (a) and (b_0)~(b_2) EDS mapping results of rGO/Ti composites SPS at 1000 ^{o}C.

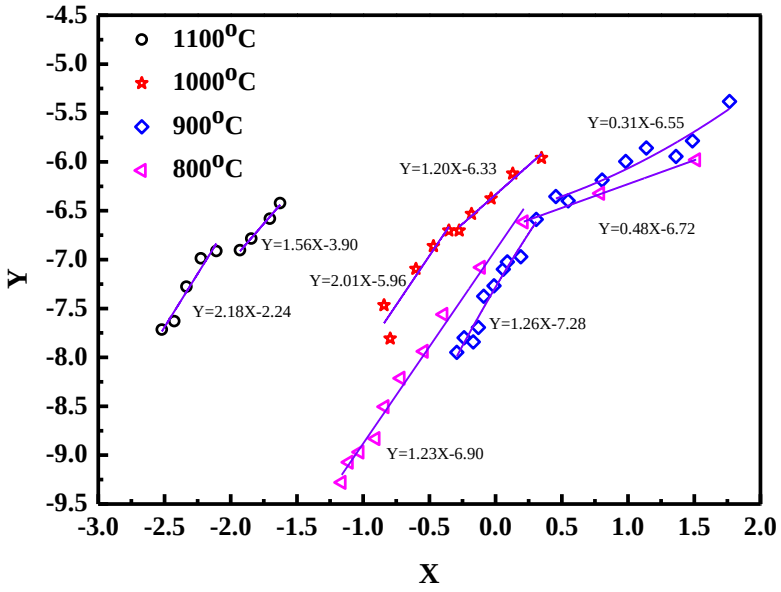

Fig. 8 Effective pressure index (n) obtained from equation (8), presented by the slope of different fitted curves.

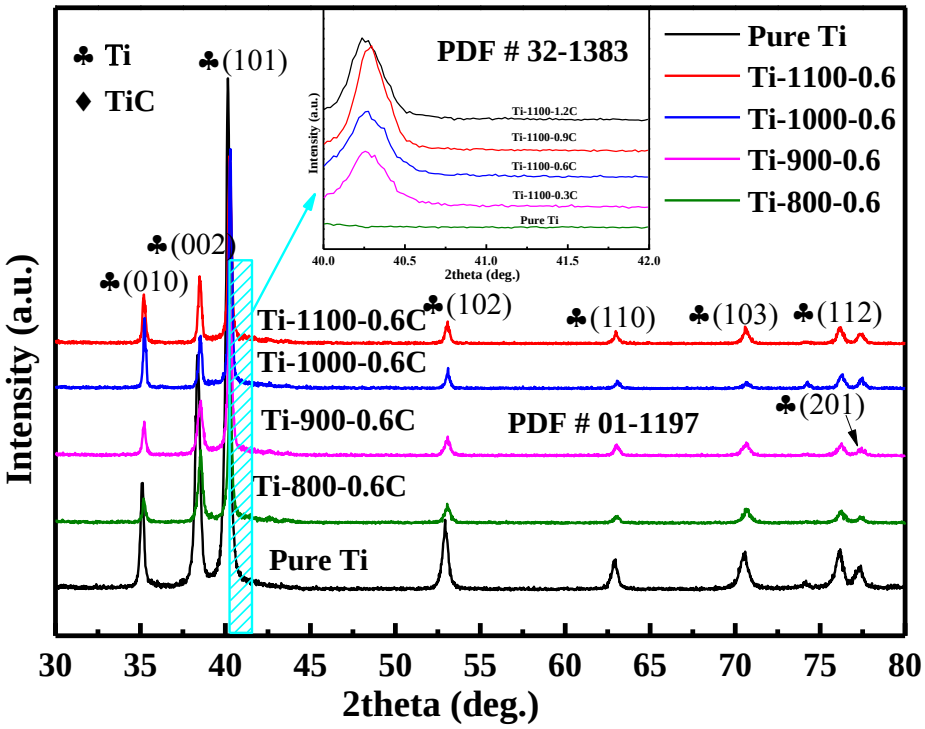

Fig. 9 XRD patterns of the rGO/Ti composites sintered at the different temperature.

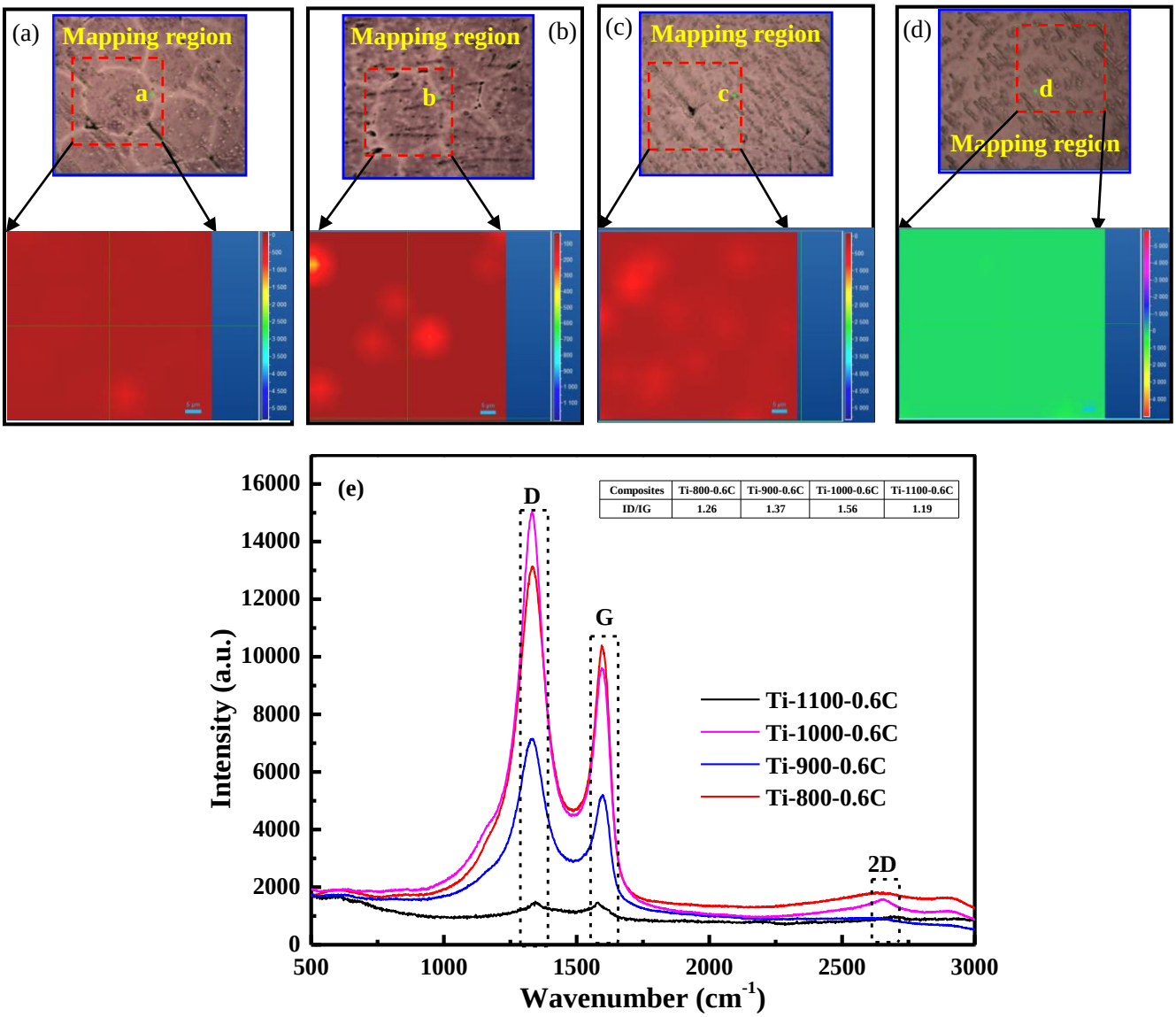

Fig. 10 Raman mapping of the 0.6wt.% rGO/Ti matrix SPSed composites at different temperature (size of 60×60 μm^2): (a) 800^{o}C; (b) 900^{o}C; (c) 1000^{o}C; (d) 1100^{o}C, (e) The Raman spectra of point a, b, c, and d which is one of the four mapping region, respectively.

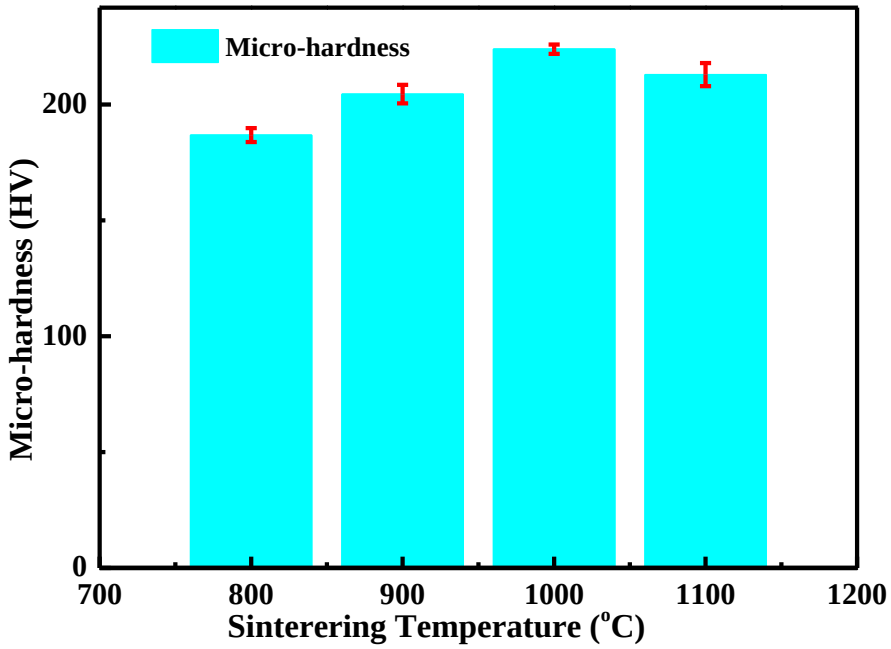

Fig. 11 Micro-hardness of rGO/Ti composites at different sintered temperatures

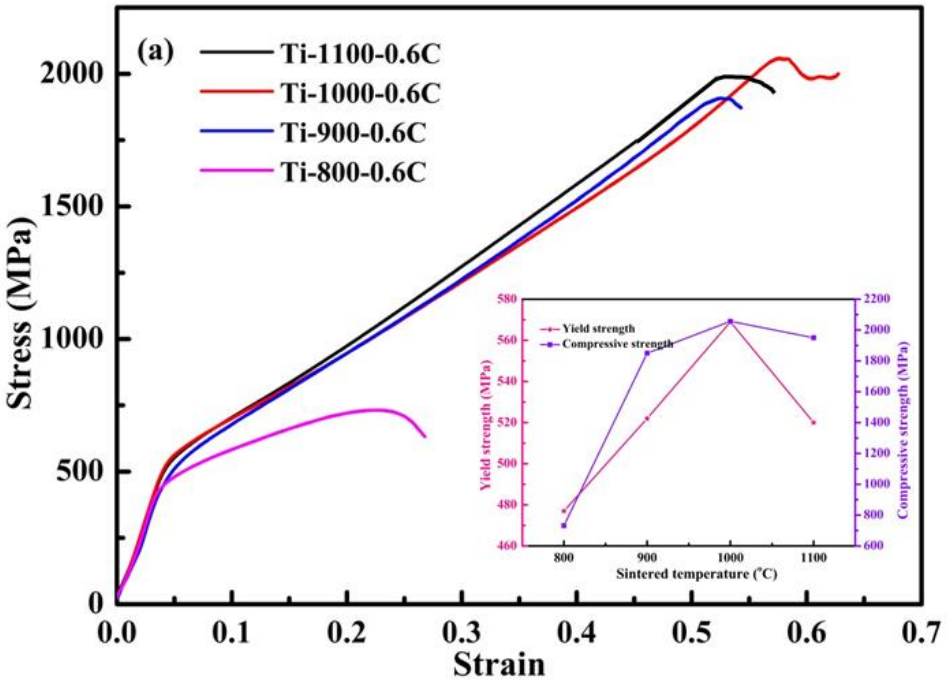

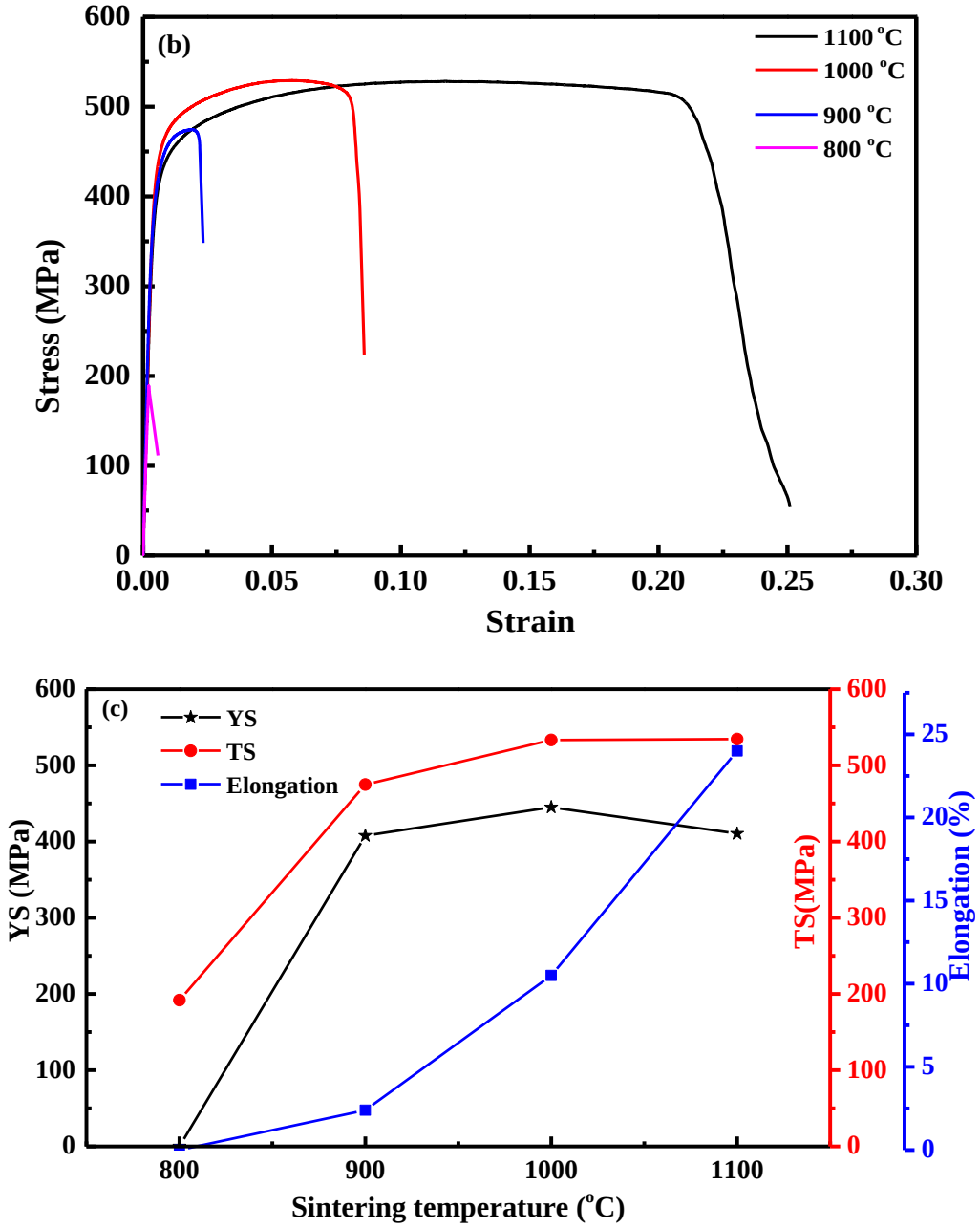

Fig. 12 (a) Compressive stress-strain curves, (b) tensile stress-strain curves and (c) the corresponding tensile properties of 0.6 wt.% rGO/Ti composites sintered at different temperatures

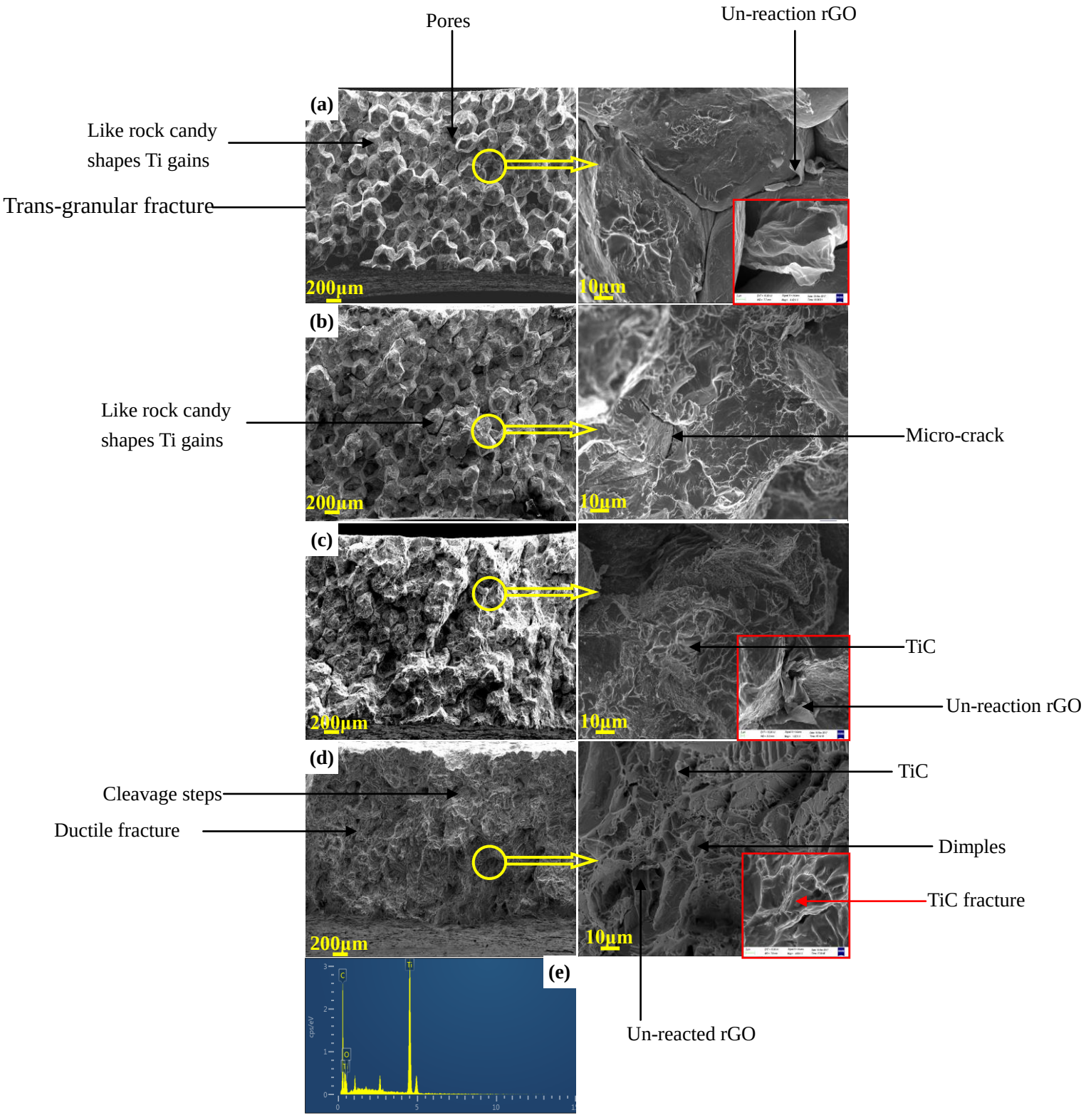

Fig. 13 SEM fracture morphology of rGO/Ti composites sintered at different temperatures: (a) 800 ^{o}C, (b) 900 ^{o}C, (c) 1000 ^{o}C, (d) 1100 ^{o}C, respectively. (e) EDS result of the red arrow positions marked in Fig. 13 (d)